

Article

A Dynamic Modeling Approach to Predict Water Inflow during Karst Tunnel Excavation

Yang Bai ^{1,2}, Zheng Wu ^{2,*} , Tao Huang ² and Daoping Peng ²

¹ School of Materials and Environmental Engineering, Chengdu Technological University, Chengdu 611730, China; yangbai0224@126.com

² Faculty of Geosciences and Environmental Engineering, Southwest Jiaotong University, Chengdu 611756, China; taohuang70@swjtu.edu.cn (T.H.); pdp0030@126.com (D.P.)

* Correspondence: elwu0017@my.swjtu.edu.cn

Abstract: During tunnel construction in strongly developed karst terrain, water inrush hazards often occur due to the complex hydrogeological conditions, which require accurate prediction of water inflow. In this study, a dynamic modeling approach for water inflow prediction of karst tunnels using the conduit flow process (CFP) is developed that considers both karst duality and changing boundary conditions of the tunnel. The CFP model has a good agreement with field-observed hydraulic head after calibration, and the Nash–Sutcliffe model efficiency (NSE) for the CFP model is 97.3%. Numerical calculation of water inflow was conducted in a successive drilling scenario with permeability change of the surrounding rocks. Additionally, a modular three-dimensional finite-difference ground-water flow model (MODFLOW) has been applied to predict the water inflow, for comparison with the CFP model. The prediction results obtained from the CFP model are generally in close agreement with the field-observed results; the percentage errors were 13.3% and 5.4%, respectively. For the MODFLOW model, the percentage errors were 34.2% and 36.8%, respectively. The proposed CFP model is both closer to reality and more reasonable than the MODFLOW model in predictive analysis of water inflow into karst tunnels, reflecting the influence of karst conduits on the water inflow process.

Keywords: karst tunnel; water inflow prediction; CFP; numerical modeling; water inrush hazards



Citation: Bai, Y.; Wu, Z.; Huang, T.; Peng, D. A Dynamic Modeling Approach to Predict Water Inflow during Karst Tunnel Excavation. *Water* **2022**, *14*, 2380. <https://doi.org/10.3390/w14152380>

Academic Editors: Shaoshuai Shi, Zongqing Zhou and Dan Ma

Received: 6 May 2022

Accepted: 29 July 2022

Published: 31 July 2022

Publisher's Note: MDPI stays neutral with regard to jurisdictional claims in published maps and institutional affiliations.



Copyright: © 2022 by the authors. Licensee MDPI, Basel, Switzerland. This article is an open access article distributed under the terms and conditions of the Creative Commons Attribution (CC BY) license (<https://creativecommons.org/licenses/by/4.0/>).

1. Introduction

High pressure and water-rich geological characteristics of strongly developed karst terrain can easily lead to water inrush during the construction of ultra-long and deep-buried tunnels. The occurrence of several disastrous events associated with water inrush into tunnels in China and elsewhere has been widely reported in recent years [1–3]. Thus, accurate prediction of water inflow into karst tunnels is an important prerequisite for ensuring the safety of tunnel construction [4,5].

Despite the difficulty of accurately predicting the water inrush during tunnel construction, a number of studies have been conducted in recent years, which mainly include empirical, analytical, experimental, numerical and stochastic methods [6]. Wang et al. developed a new type of similar material to simulate the water inrush process [7]. Zhang and Wang established a hybrid statistical learning approach to predict groundwater abundance [8]. Among them, numerical modeling has been widely used in tunnel water inflow predictions under various complicated geological conditions [9]. This method is based on groundwater hydraulics which comprehensively considers the properties of aquifers and a variety of geological information. Chiu and Chia used the modular three-dimensional finite-difference ground-water flow model (MODFLOW) to simulate the groundwater seepage field and predicted the water inflow of the tunnel using the drain package to generalize tunnel excavation; the calculated water inflow was 2.93% of the whole discharge [10]. Shi et al. employed a numerical method to simulate the water inrush process of karst tunnels under different hydraulic conditions; the relative error was 25% in predicting water inflow

and the absolute error was acceptable [11]. Chen et al. utilized the storm water management model (SWMM) to simulate the flow of karst conduit and analyzed the influence of karst conduit on the water inflow of the tunnel; the lowest relative error in prediction results was 16% [12]. Wang et al. carried out a numerical simulation on the dynamic change of the karst conduit-type water inflow process and water inflow volume, and verified the results of the numerical simulation by experimental observation [13]. However, due to the excessive simplification of the geological prototype and the neglect of the complex hydraulic properties of the karst aquifer, the prediction results of the numerical simulation of the water inflow into karst tunnels still had a large deviation from the observed values. Establishing a karst groundwater model in the study area where the tunnel is located and correctly describing its structural characteristics and water flow behavior are important prerequisites for predicting water inflow into karst tunnels [14,15].

Goldscheider et al. were the first researchers to point out that karst aquifers have distinct duality [16]. Kovács et al. divided the karst aquifer into the karst matrix and the karst conduit, and the coupling model of karst groundwater continuous conduit flow was proposed [17]. This model combined the equivalent continuum model and discrete fracture model, and took the permeability of water into account. The discrete method was employed to simulate the conduit flow with fast velocity, while the continuum method was applied to simulate the matrix flow with slow velocity, and an inherent hydraulic connection was established between them. Using the above-mentioned model, Shoemaker et al. developed the conduit flow process (CFP) model, which combined the porous media and the network of discrete conduits to simulate steady and unsteady hydrodynamic processes in karst aquifers, coupled with Darcy flow and non-Darcy flow [18]. The CFP model has been applied to several simulation studies of karst groundwater and has been verified in practice [19]. However, to the best of our knowledge, there are few reports regarding the use of the CFP model to study the prediction of water inflow into karst tunnels.

Additionally, in reality, tunnels are drilled progressively rather than instantly, and only a few studies have explicitly stated that tunnel excavation is a dynamic process with boundary conditions constantly changing. Xia et al. simulated a dynamic tunnel excavation process by altering the tunnel boundary value, leading to a more accurate prediction of the water discharge rate [20]. It is crucial for numerical modeling to take into account changes in the tunnel face location and surrounding rock permeability; however few studies about water inflow prediction into karst tunnels have considered this before, to the best of our knowledge.

Based on the above analysis, the objective of this paper is to present a dynamic modeling approach for water inflow prediction during karst tunnel construction. For this purpose, the CFP model was employed to establish the karst groundwater seepage field, and a successive drilling scenario was developed to predict the water inflow. To verify its feasibility, the CFP model as well as the MODFLOW model were applied to the Wulingshan tunnel on the QZX railway.

2. Overview of the Study Area

The study area, in Dongxi Township, Cili County, Yongding District, Zhangjiajie City, Hunan Province, belongs to the Lishui River and Yuanjiang River basins (Figure 1). It is located in the transition region of the intensively developed and moderately developed karst areas in South China, with the strong development being in the north and the weak development in the south. In this area, the morphology of the ground surface karst is varied; karst peak-cluster, karst depressions, sinkholes and caves are widely distributed, and the landform is strongly undulating with elevations ranging from 300 to 970 m above sea level. The lithology of the stratum is dominated by limestone and dolomite. A large number of karst springs and underground rivers have developed in this area; the flow rate is generally between 5.79 L/s and 34.7 L/s, with a characteristic of steep rise and fall as a result of the precipitation intensity. According to research data and field investigations there are three main conduit flows in this area: ZSX conduit flow, SHD1 conduit flow, and

SHD2 conduit flow. The flow rate of the ZSX conduit was monitored and its recession curve was analyzed. In a complete precipitation response process, the flow recession curve of the ZSX conduit flow is divided into two obvious parts (Figure 2a). The recession coefficient of the first curve is $\alpha = 0.376 \text{ d}^{-1}$, which represents the rapid discharge of large conduits or karst caves with good connectivity, large flow, fast recession, and short duration; the decay coefficient of the second segment of the curve is $\alpha = 0.043 \text{ d}^{-1}$, which represents the discharge of extensional fissures, fault fissures, and dissolved fissures with certain connectivity. In this case, the flow decay/decline speed is slow, and the duration is long. The integration calculation of each section of the decay curve can estimate the amount of water discharged for each subdomain. The calculation results showed that the discharge of karst conduits or caves accounts for 24.1% of the total discharge, and the discharge of general karst fissures, structural fissures, and pores accounts for 75.9% of the total discharge. It also suggested that the main storage spaces of karst groundwater in the ZSX basin are dissolution fissures, pores, and small karst conduits, and the large karst conduits are mostly water-conducting channels. The karst medium of the study area has apparent duality.

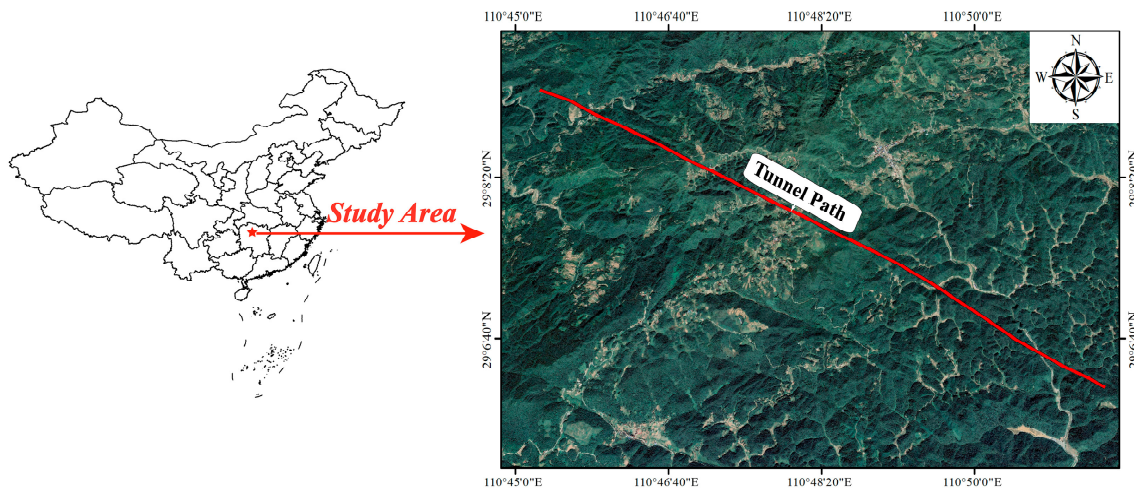


Figure 1. Location of the study area.

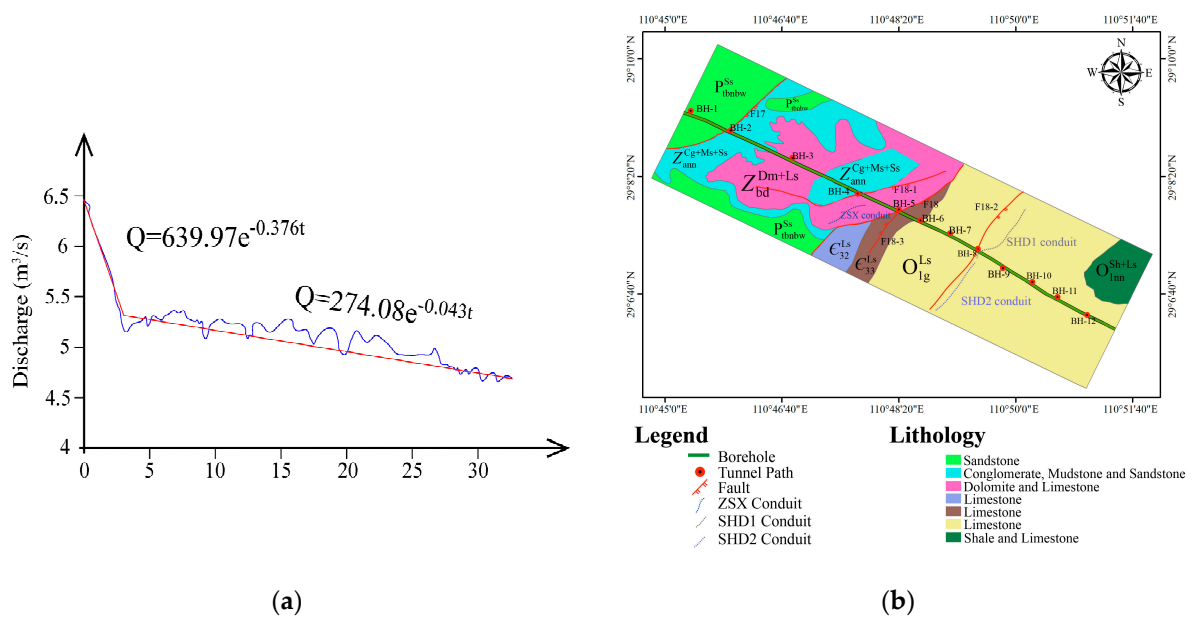


Figure 2. Hydrogeology of the study area: (a) recession curve of ZSX conduit flow; (b) lithology and hydrogeology of the tunnel area.

The mileage of the Wulingshan Tunnel is DK234+506-DK243+535, with a total length of 9029 m (Figure 2b). Limestone is the main water-bearing rock group in the survey area, with a high degree of karst terrain and water abundance. The tunnel was divided into four sections for construction, all of which were bi-directional excavations, and the groundwater inflow was measured daily. The specific excavation plan is shown in Table 1. Among them, Section 2 is located in the ZSX River basin, where the ZSX conduit is developed and Section 3 is located in the Yuanshui River basin, where the SHD1 and SHD2 conduits are developed. These two sections are located close to the conduit, and Section 3 intersects the SHD1 conduit. During construction, the risk of a water inrush hazard was extremely high due to the poor overall stability of the surrounding rock of the tunnel.

Table 1. Excavation plan of the Wulingshan tunnel.

Tunnel Section	Mileage	Section Length (m)	Excavation Days (d)
1	DK234+506- DK237+400	2894	580
2	DK237+400- DK240+060	2660	540
3	DK240+060- DK241+848	1788	360
4	DK241+848- DK243+535	1687	341

3. Modeling Approach

3.1. CFP Model

Based on the karst duality theory, the CFP model generalizes the karst aquifer into a karst matrix and a karst conduit. It also simulates the movement of steady and unsteady water flows in the two media and considers the water flow exchange between the different media (Figure 3). The water flow in the karst matrix is Darcy flow which is governed by Equation (1) as follows:

$$\frac{\partial}{\partial x} \left(K_{xx} \frac{\partial h_m}{\partial x} \right) + \frac{\partial}{\partial y} \left(K_{yy} \frac{\partial h_m}{\partial y} \right) + \frac{\partial}{\partial z} \left(K_{zz} \frac{\partial h_m}{\partial z} \right) \pm W = S_s \left(\frac{\partial h_m}{\partial t} \right) \tag{1}$$

where K is hydraulic conductivity in x , y , and z direction [LT^{-1}], h_m is the head in the karst matrix cell [L], W is the volumetric flux per unit volume [T^{-1}], S_s is the specific storage [L^{-1}], and t is time [T]. The conduit is composed of nodes and cylindrical conduits. The flow state in the conduit is divided into laminar and turbulent flow. The laminar flow state is described by the Hagen–Poiseuille Equation (2), and the turbulent flow state is depicted by the Darcy–Weisbach Equation (3). The switch between laminar flow and turbulent flow is judged by the Reynolds number, and the linear Equation (4) calculates the amount of water exchange between the karst conduit and the karst matrix.

$$Q = \frac{\pi d^4 g \Delta h_c}{128 \nu \Delta l \tau} \tag{2}$$

$$Q = \sqrt{\frac{|\Delta h_c| g d^5 \pi^2}{2 \Delta l \tau}} \log \left(\frac{2.51 \nu}{\sqrt{\frac{2 |\Delta h_c| g d^3}{\Delta l \tau}} + \frac{k_c}{3.71 d}} \right) \frac{\Delta h_c}{|\Delta h_c|} \tag{3}$$

$$Q_{ex} = \alpha_{ex} (h_c - h_m) \tag{4}$$

where Q is the volumetric flow rate [L^3T^{-1}], d is the diameter of the conduit [L], g is the acceleration of gravity [LT^{-2}], Δh_c is the head loss of the conduit [L], ν is the kinematic viscosity of water [L^2T^{-1}], τ is the tortuosity of the conduit, Δl is the length of the conduit [L], v is the mean water flow velocity [LT^{-1}], and k_c is the mean roughness height of the conduit [L].

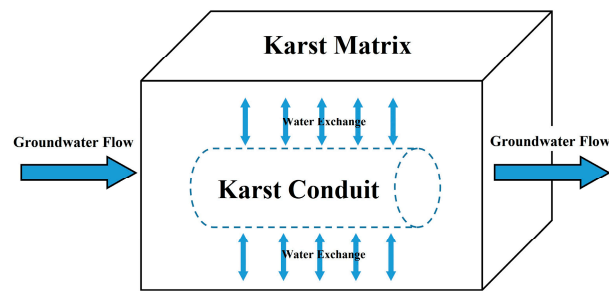


Figure 3. Schematic diagram of the CFP model.

Q_{ex} indicates the water exchange volume [L^3T^{-1}] between the conduit and the matrix, α_{ex} is the water flow exchange coefficient [L^2T^{-1}], h_c represents the water head in the conduit, and h_m denotes the matrix water head. A negative value for Q_{ex} means that the water flows from the matrix to the conduit, and a positive value for Q_{ex} means that the water flows from the conduit to the matrix.

3.2. Boundary Conditions

The model boundaries were defined by the groundwater divide and permanent rivers. Figure 4 shows the generalized diagram of the model boundary. Water flow maintained in the permanent rivers even during the excavation, thus, the Jinzhou River is the constant head boundary on the west side of the study area and the Jinzhu River is the constant head boundary on the southwest side. The east and west regions are divided into the Yuanshui and Lishui basins, and the groundwater divide is considered as a no-flow boundary of the model. On the east side of the model, the Dongxi River and Kongxian River form the constant head boundary; on the south side, there is a large karst depression called Xiangtiankeng with an average depth of 300 m, where the karst groundwater within the Yuanshui basin converges and discharges eastward along the box valley. Thus, this side was set as a no-flow boundary. Based on the boundary conditions, the site model of the study area was established, with a length of 11,800 m and a width of 5600 m.

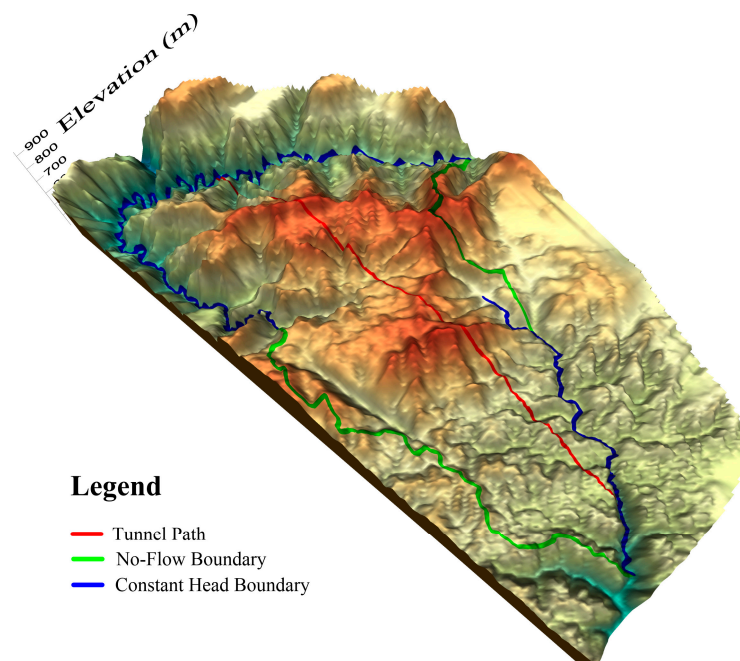


Figure 4. Boundary conditions of the study area.

3.3. Aquifer Hydraulic Properties

According to the vertical zoning of the karst hydrodynamics in the area, the model was divided into three layers vertically. The first layer is a vertical seepage zone with an average layer thickness of 200 m. The bottom elevation of the first layer was set to 700 m, with the remaining part divided into the second layer and the third layer with the water table measuring 410 m during the dry season of the area, and the bottom elevation of the model is 300 m according to the erosion base level from field investigations. Based on the geological surveying data, comprehensive lithology, and karst development, the aquifer medium in the study area was divided into nine partitions (Figure 5); numbers 1–9 were the code for identifying areas with different hydraulic conductivities. The initial hydraulic conductivity of each partition was determined based on the pumping test and empirical values.

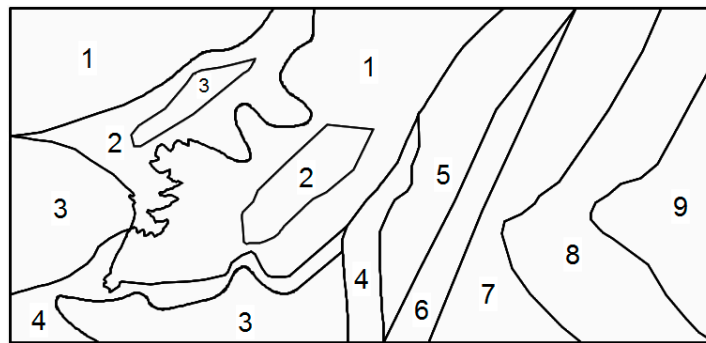


Figure 5. Partition map of hydraulic conductivity.

3.4. Conduit Parameter

There are chiefly three karst conduits in the study area, namely the ZSX conduit, the SHD1 conduit, and the SHD2 conduit. The conduit parameters involved in the CFP model are: conduit elevation, tortuosity, conduit wall roughness coefficient, conduit diameter, and the water flow exchange coefficient between the conduit and the karst matrix. Figure 6 shows that the elevations of all conduits are interpolated according to their inlet and outlet elevations, and the tortuosity of the conduit is calculated using ArcGIS 10.2 (ESRI). The diameter of the conduit is computed from the field flow monitoring, and the roughness coefficient of the conduit wall is taken from the empirical value in the strongly developed karst area [21].

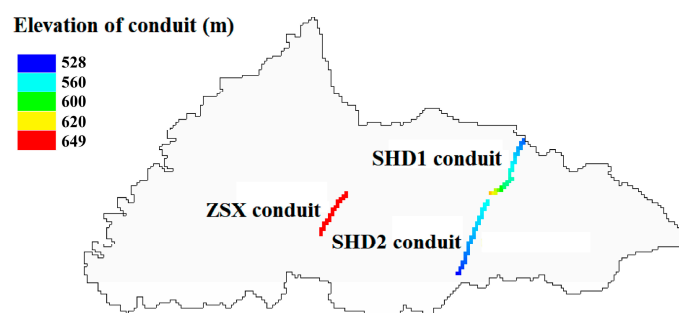


Figure 6. Conduits in the CFP model.

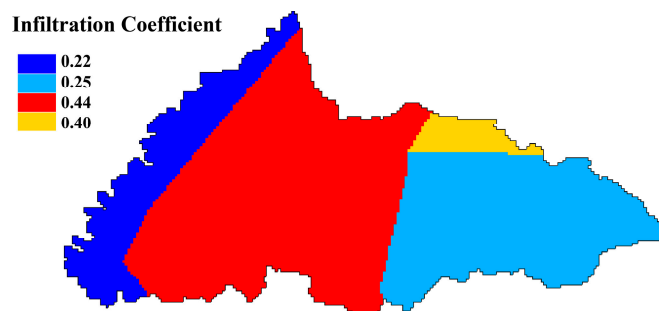
The water flow exchange coefficient is the key parameter of the CFP model. Chen et al. utilized the calculation results of the Darcy–Stokes equation of seepage and free-flow coupling to calibrate the flow equation of the CFP model [22]. The suggested value of $25 \text{ m}^2 \cdot \text{d}^{-1}$ identified in their study was taken as the exchange coefficient of the three conduits. The average annual water temperature of $16 \text{ }^\circ\text{C}$ was set as the water temperature of the model, and the Reynolds number was set as the reference value of large-scale simulation [18]. The values of the conduit parameters are shown in Table 2.

Table 2. Conduit parameters of the CFP model.

Parameters	ZSX Conduit	SHD1 Conduit	SHD2 Conduit	Unit	Explanation
DIAMETER	1.5	1.0	1.0	(m)	Conduit diameter
TORTUOSITY	1.1	1.1	1.1	-	Conduit tortuosity
RHEIGHT	0.0001	0.0001	0.0001	(m)	Conduit wall roughness
LCRITREY	2000	2000	2000	-	Reynolds number
TCRITREY	4000	4000	4000	-	Reynolds number
K_EXCHANGE	25	25	25	(m ² ·d ⁻¹)	Exchange coefficient

3.5. Model Representation

The surface elevation of the model was derived from a topographic raster map. The total area of the model domain is approximately 66.08 km² and the finite difference grid was divided into 236 columns and 112 rows with a computational cell size of 50 m × 50 m. The study area has abundant rainfall, with an average annual precipitation of 1734 mm and an annual average evaporation of 1286 mm during the hydrometeorological monitoring period. From April to September of every year is considered the wet season, while the dry season can last from October to March of the following year. Because there is no concentrated irrigation recharge and groundwater exploitation in the area, groundwater discharge is controlled by the Jinzhu River, Dongxi River, Toudaogou River, and Kongxian River. The only recharge of groundwater in the area is from precipitation, including two recharge ways of diffuse recharge to the matrix, and concentrated recharge to the conduit. The amount of diffuse recharge can be calculated by the rainfall infiltration coefficient, and the rainfall infiltration coefficient in karst areas is related to the surface morphology and rainfall characteristics [23]. Based on the distribution of karst depressions in the study area, four infiltration zones were determined, whose rainfall, underground river, and spring discharge were monitored. The infiltration coefficient of each zone was calculated according to the water balance principle (Figure 7).

**Figure 7.** Partition map of infiltration coefficient.

The concentrated recharge implies that the runoff enters the doline or the karst sink-hole under the condition of storm rainfall, and directly recharges the karst conduit. Borghi mentioned that the components of concentrated recharge cannot be ignored in the simulation of karst groundwater flow, and there is a certain proportional relationship between concentrated recharge and precipitation intensity [24]. By monitoring the precipitation in the study area and the recharge amount of each conduit in the dolines and outlets, the proportion of concentrated recharge under different precipitation conditions was determined (Table 3).

Table 3. Proportion of concentrated recharge for conduits.

Precipitation (mm)	Duration (h)	Maximum Intensity (mm·h ⁻¹)	Average Intensity (mm·h ⁻¹)	Proportion of Concentrated Recharge		
				ZSX Conduit	SHD1 Conduit	SHD2 Conduit
114.2	42	21.6	2.719	0.571	0.536	0.554
64.4	36	10.8	1.79	0.440	0.422	0.432
64	63	12.6	1.02	0.128	0.137	0.184
355.2	142	23.2	2.501	0.518	0.476	0.503
216.8	58	13.2	3.576	0.677	0.636	0.652
34.8	16	15.6	2.175	0.473	0.442	0.492

The groundwater seepage field was set up for a 10-year simulation period, which was divided equally into 20 modeling periods, according to the wet and dry seasons. Each modeling period was further divided into six time steps with a month-long simulating time under steady flow. Considering that there is a significant linear relationship between groundwater level and surface elevation [25], regression analysis was conducted between the groundwater level and the corresponding surface elevation of the boreholes. The results are shown in Figure 8; the correlation coefficient of R^2 was up to 0.94, and the linear regression equation was as follows:

$$h = 0.9348E + 3.3614 \tag{5}$$

where E stands for the surface elevation and h denotes the initial groundwater level. Equation (5) was used to set the initial groundwater level of all cells in the model.

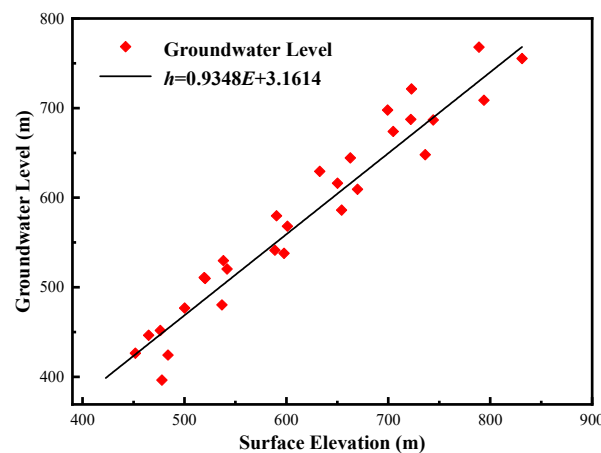


Figure 8. Linear regression analysis.

3.6. Dynamic Excavation

In this study, the drain package (DRN) was utilized to generalize the water inflow during and after tunnel excavation, which involved two parameters: the drainage elevation and the drainage coefficient. The drainage elevation is the elevation of the tunnel axis, and the drainage coefficient is determined by the permeability of the surrounding rock. Tunnel excavation is a dynamic process. As the tunnel face moves forward, the boundary conditions of the tunnel subsequently change. However, existing research does not fully consider the tunnel excavation process and permeability change of the surrounding rock. Therefore, this study developed a dynamic modeling approach based on the tunnel excavation scheme. Before the tunnel is excavated to a certain cell, the cell is considered to be an ordinary active cell. Once excavated, the cell is immediately set as the DRN cell, and the drainage coefficient is the permeability coefficient of the cell (Figure 9).

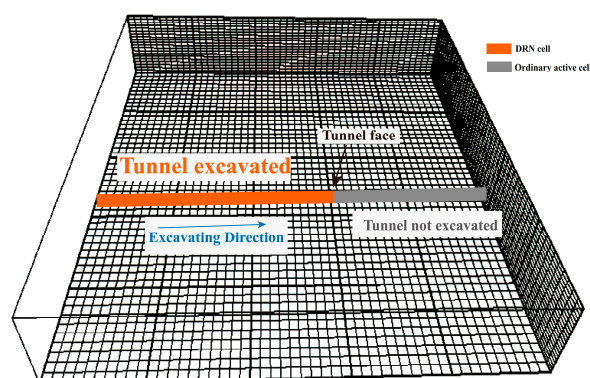


Figure 9. Concept plot of the dynamic excavation model.

At the same time, the disturbance of the surrounding rock caused by the tunnel excavation is considered. That is, the equivalent permeability of the surrounding rock within the range of 0.5–1 times the diameter of the tunnel will be reduced to between 1/5 and 1/10 of the initial state after the tunnel is excavated [26]. The equivalent radius of the tunnel is 6.9 m, and the average speed of tunnel excavation is 2.5 m/d, thus, the width of tunnel is set to 25 m considering the disturbed surrounding rock, and the drainage coefficient becomes 1/10 of the original, after a 10-day excavation period. The tunnel unit is refined to a 25 m × 25 m × 25 m cubic cell, where each cell represents the completion of one excavation, and the tunnel lining installation is conducted every 70 m of the excavation. Consequently, the drainage coefficient of the DRN cell becomes 8.64×10^{-3} m/d on the 18th day after one excavation [27].

The tunnel units were set in columns 30 to 391 of the model, involving 362 cells in total. The average tunnel elevation was 420 m, and a layer the thickness of 25 m was vertically subdivided in the model, with the tunnel as the fourth layer of the model. We employed ModelMuse [28], developed by USGS, as the visual processing tool of the model, and then we compiled the parameters of the DRN cells using ArcGIS 10.2 (ESRI) and imported them into the dataset of ModelMuse to assign the correlated cells. According to the proposed dynamic modeling approach and tunnel excavation plan, each modeling time step had a 10-day time simulation with an unsteady state flow.

4. Results and Discussion

4.1. Model Calibration

The hydrogeological parameters in the groundwater numerical model are uncertain, thus, it is necessary to check the parameters of the modeling to obtain reasonable numerical simulation results. In this study, the parameters were calibrated automatically using the UCODE program [29]. The data were taken from the monthly monitored water level of boreholes in the area, including a total of 58 parameters such as conduit diameter, roughness coefficient of the conduit wall, conduit tortuosity, water flow exchange coefficient, and hydraulic conductivities of the model. Although there are many parameters, not all of them have a significant impact on the simulation results. Therefore, a sensitivity analysis should be performed for all parameters to find out the most sensitive and important parameters for model calibration.

Figure 10 exhibits the calculation results of a comprehensive sensitivity analysis for parameters with high sensitivity. The conduit diameter had the greatest influence on the simulation results, followed by the conduit tortuosity. The comprehensive scaling sensitivity of the flow exchange coefficient and the conduit wall roughness were 0.1 and 0.045, respectively, which had little influence on the model compared with other parameters. The range of comprehensive scaling in the sensitivity analyses of all parameters was 0.001897 to 103.7189. Hill et al. reported that when the sensitivity of a parameter is smaller than 0.01 of the maximum sensitivity, this parameter can be ignored in the process of model calibration [30]. Therefore, the parameters with a sensitivity of less than 1.037 were

not corrected. Furthermore, the calibration of the model should follow the principle of not changing the objective properties of hydrogeological elements. Considering that the conduit properties such as conduit diameter were obtained from the actual survey, we only corrected the hydraulic conductivities; once there is more than an order of magnitude difference between the calibrated hydraulic conductivity and that of the pumping test, the value should be re-corrected. The parameter results are shown in Table 4.

Table 4. Calibration results of hydraulic conductivities.

Hydraulic Conductivity	Initial Value (m·d ⁻¹)	Calibrated Value (m·d ⁻¹)
HK_Zbd2	0.4	0.667
HK_Zbd1	0.13	0.125
HK_Zan2	0.1	0.413
HK_O42	0.2	0.137
HK_O21	0.3	0.3
HK_Zan1	0.4	0.16
HK_O22	0.3	0.37
VK_Zan2	0.01	0.011
HK_O41	0.1	0.177
HK_Cam1	0.3	0.284
VK_Pt2	0.01	0.011
HK_Pt2	0.1	0.457
HK_Pt1	0.25	0.5
HK_O32	0.4	0.403
HK_O12	0.1	0.15
HK_OS2	0.4	0.2
HK_Cam2	0.2	0.25
VK_Zbd2	0.04	0.04
HK_O31	0.2	0.2
HK_O11	0.1	0.141
VK_O22	0.01	0.037
HK_OS1	0.2	0.21
VK_OS2	0.04	0.093
VK_O42	0.02	0.02
VK_Zbd1	0.16	0.63
VK_O12	0.01	0.015
HK_Zan3	0.01	0.01
VK_Cam2	0.04	0.025
VK_O32	0.04	0.04

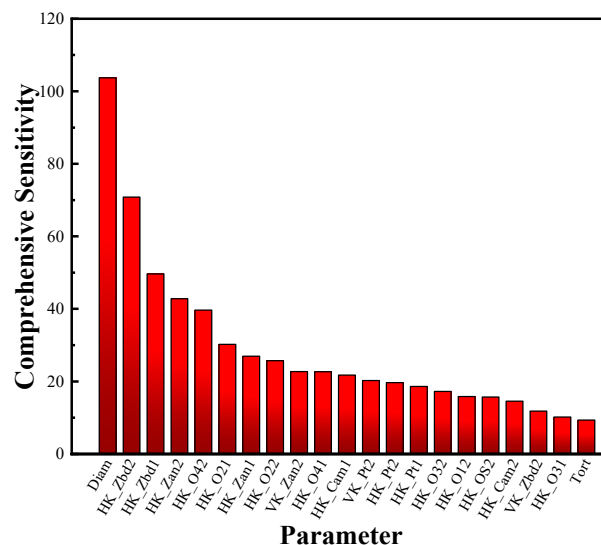


Figure 10. Composite scaled sensitivity.

$$\text{NSE} = 1 - \frac{\sum_{t=1}^T (h_o^t - h_s^t)^2}{\sum_{t=1}^T (h_o^t - \bar{h}_o)^2} \quad (6)$$

$$R^2 = \frac{\sum_{t=1}^T (h_o^t - \bar{h}_o)(h_s^t - \bar{h}_s)}{\sqrt{\sum_{t=1}^T (h_o^t - \bar{h}_o)^2} \sqrt{\sum_{i=1}^n (h_s^i - \bar{h}_s)^2}} \quad (7)$$

Equations (6) and (7) are the calculation formulas for the Nash–Sutcliffe efficiency (NSE) and coefficient of determination (R^2), respectively, which are employed to assess the goodness of fit of the model [31]. In the above equations, h_s^t is the simulated value of hydraulic head at the time of t , h_o^t is the observed value of hydraulic head at the time of t , \bar{h}_o is the mean value of observed hydraulic heads, \bar{h}_s is the mean value of simulated hydraulic heads, and T is the final simulation time. The R^2 ranges between 0 and 1, where one means that the simulated value is equal to the observed value and zero means that there is no correlation between the simulated and observed values.

As shown in the 1:1 line fitting diagram (Figure 11a), the calibration results showed good model performance when the value of R^2 was 0.991 and the corresponding NSE was 97.3%, respectively. Figure 11b displays the hydraulic head distribution of the study area before tunnel excavation, which served as the initial groundwater seepage field for water inflow prediction.

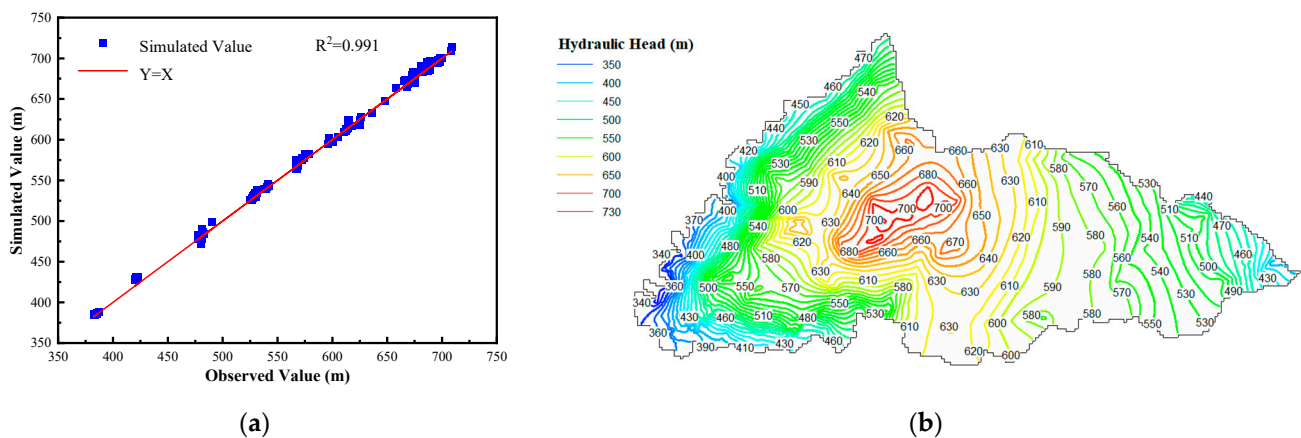


Figure 11. Calibrated CFP model: (a) comparison of simulated and observed hydraulic heads; (b) calibrated groundwater seepage field of the study area.

4.2. Water Inflow Prediction

The water inflow of the tunnel was calculated using the computer program ZONEBUDGET [32]. After activating the ZONEBUDGET option of the cells above and cells on both sides of the tunnel, the water budget calculation in all DRN cells served as the water inflow prediction results. For comparison, the groundwater seepage field of the study area was established to predict the water inflow with the same hydraulic properties and successive excavation scenario, using a MODFLOW model without the karst conduits.

Section 2 is located in the ZSX River basin, where the ZSX conduit flow is developed. The value of mean absolute error was $2932.62 \text{ m}^3 \cdot \text{d}^{-1}$ according to the CFP model prediction, and the MODFLOW model prediction had a greater mean absolute error value of $3984.88 \text{ m}^3 \cdot \text{d}^{-1}$. The water inflow curve in Section 2 has obvious rise and decay trends. During the wet season, the water in the matrix will be recharged by the karst conduit with the increase of conduit flow, and the matrix cells of the model will additionally be recharged [33,34]. Figure 12a shows that the prediction results of the MODFLOW model

are smaller than the measured data because it only has matrix cells, while the CFP model prediction results are closer to the actual water inflow. In the dry season, karst conduits will “snatch” the water volume of the matrix due to the reduction of precipitation recharge, resulting in an additional drop of water volume from the matrix cell. Since there is no conduit cell in the MODFLOW model, the prediction results were too large to meet good agreement with the measured water inflow, even though it could reflect its downward trend, while the prediction results of the CFP model were closer to the observed value. The peak value of water inflow in this section was up to $15,897.14 \text{ m}^3 \cdot \text{d}^{-1}$, and the corresponding value of the CFP model prediction was $13,782.35 \text{ m}^3 \cdot \text{d}^{-1}$, indicating a percentage error of 13.3%. The prediction value of the MODFLOW model was $10,453.827 \text{ m}^3 \cdot \text{d}^{-1}$ with a percentage error of 34.2%. Thus, the statistical results demonstrated that the predicted value of the CFP model was closer to the actual water inflow, reflecting the characteristics of the water inflow time series.

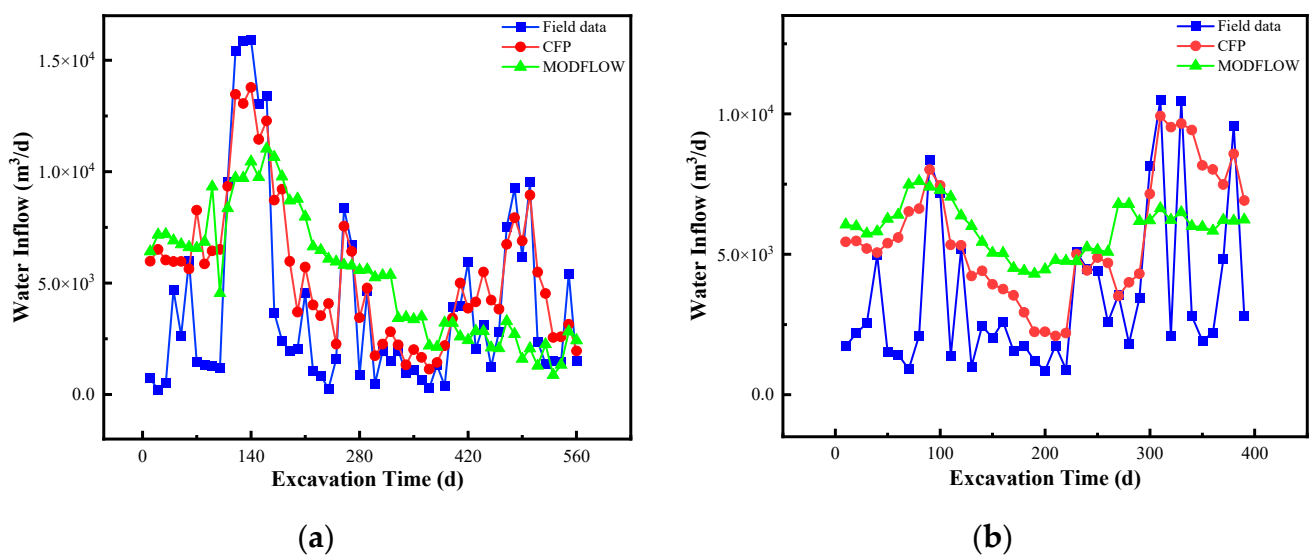


Figure 12. Water inflow prediction results: (a) Section 2; (b) Section 3.

Section 3 is located in the Yuanshui River basin, where SHD1 and SHD2 conduit flows are developed. The value of mean absolute error was $2325.66 \text{ m}^3 \cdot \text{d}^{-1}$ according to the CFP model prediction, with a larger value of $3162.99 \text{ m}^3 \cdot \text{d}^{-1}$ by the MODFLOW model (Figure 12b). The tunnel path intersects the SHD1 conduit at DK241+012, 103 m above the tunnel. When the tunnel was excavated to this position, the peak field value of the water inflow was up to $10,492.00 \text{ m}^3 \cdot \text{d}^{-1}$ in the entire section. The corresponding CFP model predicted value was $9921.97 \text{ m}^3 \cdot \text{d}^{-1}$ with a percentage error of 5.4%, while the prediction result by the MODFLOW model was $6634.56 \text{ m}^3 \cdot \text{d}^{-1}$ with a percentage error of 36.8%. When the tunnel was excavated underneath the karst conduit, the water inflow increased sharply. The conduit cell of the CFP model provided water volume to the matrix cell as an additional recharge and described the dynamic and sharp increase of water inflow in this section more accurately. Since there are no conduit cells in the MODFLOW model and the excavation time is at the end of the tunnel construction, the matrix cells within the tunnel area tend to be dry. The characteristics of “sudden rise and fall” of water inrush into the tunnel cannot be described by the MODFLOW model, thus, the prediction results were in poor agreement with the observed values.

Through the analysis of the prediction results of these two sections, the CFP model based on karst duality was able to reflect the influence of conduit flow on the water inflow into the karst tunnel. However, the MODFLOW model only has matrix elements. When the MODFLOW model was used to predict the water inflow into the tunnel, the influence of karst characteristics such as conduit flow on water inflow were ignored. Therefore, there

are great advantages to utilizing the CFP model to predict the water inflow of karst tunnels in areas with highly developed karst features and strong karst duality.

5. Conclusions

This paper established a dynamic modeling approach based on the CFP model to predict the water inflow into the Wulingshan tunnel during excavation. The main conclusions of this paper are summarized as follows:

According to the duality of the karst terrain in the study area, a CFP model was employed to establish the groundwater seepage field. After the sensitivity analysis and calibration, the calibrated CFP model showed good performance with $R^2 = 0.991$ and an NSE of 97.3%, which indicated that the CFP model successfully simulated the characteristics of karst groundwater flow.

We developed a dynamic drilling approach considering the permeability changes of the surrounding rock during the excavating process for predicting the water inflow into the Wulingshan tunnel. Prediction results of the CFP model displayed percentage errors of 13.3% and 5.4% of the maximum water inflow rate in Sections 2 and 3, respectively. Compared with the MODFLOW model, the CFP model had better accuracy, indicating that it could show the influence of karst conduits on water inflow into the karst tunnel.

This study considered the influence of the duality of karst groundwater and the dynamic characteristics of tunnel excavation, which show better performance in the prediction of water inflow into karst tunnels with strong dual characteristics. The multi-field coupling mechanism in the CFP model will be considered and deepened in the next relevant study.

Author Contributions: Conceptualization, Z.W.; methodology, Z.W.; software, T.H. and Y.B.; investigation, D.P.; resources, T.H.; data curation, Y.B. and Z.W.; writing—original draft preparation, Y.B. and Z.W.; writing—review and editing, Y.B. and Z.W. All authors have read and agreed to the published version of the manuscript.

Funding: This research was funded by the National Natural Science Foundation of China (U1734205).

Data Availability Statement: The data used in this study are available from the corresponding authors upon request.

Conflicts of Interest: The authors declare no conflict of interest.

References

1. Zhang, N.; Shen, S.L.; Zhou, A.; Arulrajah, A. Tunneling Induced Geohazards in Mylonitic Rock Faults with Rich Groundwater: A Case Study in Guangzhou. *Tunn. Undergr. Space Technol.* **2017**, *74*, 262–272. [[CrossRef](#)]
2. Zhang, N.; Zheng, Q.; Elbaz, K.; Xu, Y.S. Water Inrush Hazards in the Chaoyang Tunnel, Guizhou, China: A Preliminary Investigation. *Water* **2020**, *12*, 1083. [[CrossRef](#)]
3. Yang, W.; Fang, Z.; Yang, X.; Shi, S.; Wang, J.; Wang, H.; Bu, L.; Li, L.; Zhou, Z.; Li, X. Experimental Study of Influence of Karst Aquifer on the Law of Water Inrush in Tunnels. *Water* **2018**, *10*, 1211. [[CrossRef](#)]
4. Xue, Y.; Teng, T.; Zhu, L.; He, M.; Ren, J.; Dong, X.; Liu, F. Evaluation of the Non-Darcy Effect of Water Inrush from Karst Collapse Columns by Means of a Nonlinear Flow Model. *Water* **2018**, *10*, 1234. [[CrossRef](#)]
5. Song, J.; Chen, D.; Wang, J.; Bi, Y.; Liu, S.; Zhong, G.; Wang, C. Evolution Pattern and Matching Mode of Precursor Information about Water Inrush in a Karst Tunnel. *Water* **2021**, *13*, 1579. [[CrossRef](#)]
6. Li, S.C.; Zhou, Z.Q.; Li, L.P.; Xu, Z.H.; Zhang, Q.Q.; Shi, S.S. Risk Assessment of Water Inrush in Karst Tunnels Based on Attribute Synthetic Evaluation System. *Tunn. Undergr. Space Technol.* **2013**, *38*, 50–58. [[CrossRef](#)]
7. Wang, Z.; Zhang, Q.; Shao, J.; Zhang, W.; Wu, X.; Zhu, X. New Type of Similar Material for Simulating the Processes of Water Inrush from Roof Bed Separation. *ACS Omega* **2020**, *5*, 30405–30415. [[CrossRef](#)]
8. Zhang, Q.; Wang, Z. Spatial Prediction of Loose Aquifer Water Abundance Mapping Based on a Hybrid Statistical Learning Approach. *Earth Sci. Inform.* **2021**, *14*, 1349–1365. [[CrossRef](#)]
9. Hwang, J.H.; Lu, C.C. A Semi-Analytical Method for Analyzing the Tunnel Water Inflow. *Tunn. Undergr. Space Technol.* **2007**, *22*, 39–46. [[CrossRef](#)]
10. Chiu, Y.C.; Chia, Y. The Impact of Groundwater Discharge to the Hsueh-Shan Tunnel on the Water Resources in Northern Taiwan. *Hydrogeol. J.* **2012**, *20*, 1599–1611. [[CrossRef](#)]
11. Shi, W.H.; Yang, T.H.; Liu, H.L.; Yang, B. Numerical Modeling of Non-Darcy Flow Behavior of Groundwater Outburst through Fault Using the Forchheimer Equation. *J. Hydrol. Eng.* **2018**, *23*, 04017062. [[CrossRef](#)]

12. Chen, D.; Xu, M.; Zeng, K.; Zhao, R. Analysis of the dynamic change process of water inflow in karst tunnel simulated by SWMM model—Take Zhongba Tunnel as an example. *Ground Water* **2014**, *36*, 82–84. (In Chinese)
13. Wang, J.H.; Li, S.C.; Li, L.P.; Xu, Z.H. Dynamic evolution characteristics and prediction of water inflow of karst piping-type water inrush of tunnels. *Chin. J. Geotech. Eng.* **2018**, *40*, 1880–1888. (In Chinese)
14. Li, S.C.; He, P.; Li, L.P.; Shi, S.S.; Zhang, Q.Q.; Zhang, J.; Hu, J. Gaussian Process Model of Water Inflow Prediction in Tunnel Construction and Its Engineering Applications. *Tunn. Undergr. Space Technol.* **2017**, *69*, 155–161. [[CrossRef](#)]
15. Zhang, P.X.; Huang, Z.; Liu, S.; Xu, T.S. Study on the Control of Underground Rivers by Reverse Faults in Tunnel Site and Selection of Tunnel Elevation. *Water* **2019**, *11*, 889. [[CrossRef](#)]
16. Goldscheider, N.; Drew, D. *Methods in Karst Hydrogeology*, 1st ed.; Taylor and Francis: London, UK, 2007; pp. 33–47.
17. Kovács, A.; Perrochet, P.; Király, L.; Jeannin, P.Y. A Quantitative Method for the Characterisation of Karst Aquifers Based on Spring Hydrograph Analysis. *J. Hydrol.* **2005**, *303*, 152–164. [[CrossRef](#)]
18. Shoemaker, W.B.; Kuniatsky, E.L.; Birk, S.; Bauer, S.; Swain, E.D. Documentation of a Conduit Flow Process (CFP) for MODFLOW-2005. *U.S. Geol. Surv. Tech. Methods* **2008**, *6*, 50.
19. Chang, Y.; Wu, J.; Jiang, G.; Kang, Z. Identification of the Dominant Hydrological Process and Appropriate Model Structure of a Karst Catchment through Stepwise Simplification of a Complex Conceptual Model. *J. Hydrol.* **2017**, *548*, 75–87. [[CrossRef](#)]
20. Xia, Q.; Xu, M.; Zhang, H.; Zhang, Q.; Xiao, X.X. A Dynamic Modeling Approach to Simulate Groundwater Discharges into a Tunnel from Typical Heterogenous Geological Media during Continuing Excavation. *KSCE J. Civ. Eng.* **2018**, *22*, 341–350. [[CrossRef](#)]
21. Zhao, L.J.; Xia, R.Y.; Yang, Y.; Shao, J.L.; Cao, J.W.; Fan, L.J. Research on Numerical Simulation of Karst Conduit Media Based on CFP: A Case Study of Zhaidi Karst Underground River Subsystem of Guilin. *Acta Geosci. Sin.* **2018**, *39*, 225–232. (In Chinese)
22. Chen, N.; Gunzburger, M.; Hu, B.; Wang, X.; Woodruff, C. Calibrating the Exchange Coefficient in the Modified Coupled Continuum Pipe-Flow Model for Flows in Karst Aquifers. *J. Hydrol.* **2012**, *414*, 294–301. [[CrossRef](#)]
23. Yi, L.X.; Xia, R.Y.; Wang, Z.; Lu, H.P.; Zhao, L.J. Infiltration coefficient of precipitation in karst peak-cluster depression area: A case study of Zhaidi karst underground river basin. *Arsologica Sin.* **2017**, *36*, 512–517. (In Chinese)
24. Borghi, A.; Renard, P.; Cornaton, F. Can One Identify Karst Conduit Networks Geometry and Properties from Hydraulic and Tracer Test Data? *Adv. Water Resour.* **2016**, *90*, 99–115. [[CrossRef](#)]
25. Panagopoulos, G. Application of MODFLOW for Simulating Groundwater Flow in the Trifilia Karst Aquifer, Greece. *Environ. Earth Sci.* **2012**, *67*, 1877–1889. [[CrossRef](#)]
26. Fernandez, G.; Moon, J. Excavation-Induced Hydraulic Conductivity Reduction around a Tunnel—Part 1: Guideline for Estimate of Ground Water Inflow Rate. *Tunn. Undergr. Space Technol.* **2010**, *25*, 560–566. [[CrossRef](#)]
27. Li, Z.; He, C.; Yang, S.Z.; Wang, B.; Wang, J.Y. Experimental study on tunnel inflow without considering the influence of excavation disturbance. *Chin. J. Geotech. Eng.* **2016**, *35*, 2499–2506. (In Chinese)
28. Winston, R.B. ModelMuse version 4: A graphical user interface for MODFLOW 6. *U.S. Geol. Surv. Tech. Methods* **2019**, *5036*, 10.
29. Poeter, E.P.; Hill, M.C. UCODE, a Computer Code for Universal Inverse Modeling. *Comput. Geosci.* **1999**, *25*, 457–462. [[CrossRef](#)]
30. Hill, M.C.; Tiedeman, C.R. *Effective Groundwater Model Calibration: With Analysis of Data, Sensitivities, Predictions, and Uncertainty*, 1st ed.; John Wiley & Sons: Hoboken, NJ, USA, 2006; pp. 96–107.
31. Nash, J.E.; Sutcliffe, J.V. River flow forecasting through conceptual models part I—A discussion of principles. *J. Hydrol.* **1970**, *10*, 282–290. [[CrossRef](#)]
32. Harbaugh, A.W. Zonebudget Version 3.01, A Computer Program for Computing Subregional Water Budgets for MODFLOW Ground-Water Flow Models. *US Geol. Surv. Groundw. Softw.* **2009**, *46*, 90–392.
33. Bailly-Comte, V.; Martin, J.B.; Jourde, H.; Sreaton, E.J.; Pistre, S.; Langston, A. Water Exchange and Pressure Transfer between Conduits and Matrix and Their Influence on Hydrodynamics of Two Karst Aquifers with Sinking Streams. *J. Hydrol.* **2010**, *386*, 55–66. [[CrossRef](#)]
34. Binet, S.; Joigneaux, E.; Pauwels, H.; Albéric, P.; Fléhoc, C.; Bruand, A. Water Exchange, Mixing and Transient Storage between a Saturated Karstic Conduit and the Surrounding Aquifer: Groundwater Flow Modeling and Inputs from Stable Water Isotopes. *J. Hydrol.* **2017**, *544*, 278–289. [[CrossRef](#)]